

A Sub-Damped Ly α Absorber with Unusual Abundances:
Evidence of Gas Recycling in a Low-Redshift Galaxy Group

BRENDA L. FRYE,¹ DAVID V. BOWEN,² TODD M. TRIPP,³ EDWARD B. JENKINS,⁴ MAX PETTINI,⁵ AND SARA L. ELLISON⁶

¹*Department of Astronomy/Steward Observatory, University of Arizona, 933 N Cherry Ave., Tucson, AZ 85721, USA*

²*Department of Astrophysical Sciences, Princeton University, Princeton, NJ 08544, USA*

³*Department of Astronomy, University of Massachusetts, Amherst, MA 01003, USA*

⁴*Department of Astrophysical Sciences, Princeton University, Princeton, NJ 08544*

⁵*Institute of Astronomy, Madingley Rd., Cambridge CB3 0HA, UK*

⁶*Department of Physics and Astronomy, University of Victoria, PO Box 1700 STN CSC, Victoria, BC, V8W 2Y2, Canada*

ABSTRACT

Using *Hubble Space Telescope/Space Telescope Imaging Spectrograph* G140M spectroscopy, we investigate an absorption-line system at $z=0.07489$ in the spectrum of the quasi-stellar object PG 1543+489 ($z_{\text{QSO}}=0.401$). The sightline passes within $\rho = 66$ kpc of an edge-on $2L^*$ disk galaxy at a similar redshift, but the galaxy belongs to a group with four other galaxies within $\rho = 160$ kpc. We detect H I [$\log N(\text{H I}/\text{cm}^{-2}) = 19.12 \pm 0.04$] as well as N I, Mg II, Si II, and Si III, from which we measure a gas-phase abundance of $[\text{N}/\text{H}] = -1.0 \pm 0.1$. Photoionization models indicate that the nitrogen-to-silicon relative abundance is solar, yet magnesium is underabundant by a factor of ≈ 2 . We also report spatially resolved emission-line spectroscopy of the nearby galaxy, and we extract its rotation curve. The galaxy’s metallicity is $\approx 8\times$ higher than $[\text{N}/\text{H}]$ in the absorber, and interestingly, the absorber velocities suggest that the gas at $\rho = 66$ kpc is corotating with the galaxy’s stellar disk, possibly with an inflow component. These characteristics could indicate that this sub-damped Ly α absorber system arises in a “cold-accretion” flow. However, the absorber abundance patterns are peculiar. We hypothesize that the gas was ejected from its galaxy of origin (or perhaps is a result of tidal debris from interactions between the group galaxies) with a solar nitrogen abundance, but that subsequently mixed with (and was diluted by) gas in the circumgalactic medium (CGM) or group. If the gas is bound to the nearby galaxy, this system may be an example of the gas “recycling” predicted by theoretical galaxy simulations. Our hypothesis is testable with future observations.

Keywords: quasars: absorption lines—quasars: individual (PG 1543+489)—galaxies: halos — intergalactic medium

1. INTRODUCTION

Complex physics drives and regulates star formation in the inner regions of galaxies. In addition, it is now recognized that a variety of processes on larger scales also have important functions in galaxy formation and evolution. Galaxies must continue to accrete gas from the intergalactic medium (IGM) in order to explain their sustained star-formation histories. Accreting gas could be shock-heated to the virial temperature as it drops into a galaxy, but it has also been shown that the gas can radiatively cool and maintain a much lower temperature as it falls in, the so-called “cold mode” accretion (Birnboim & Dekel 2003; Kereš et al. 2005). The detailed physics that occurs in accreting gas can profoundly affect fundamental galactic properties (e.g., Maller & Bullock 2004; McCourt et al. 2012; Voit et al. 2017). Conversely, outflows and “feedback” propelled by star formation or active galactic nuclei (AGNs; see, e.g., Veilleux et al. 2005) can regulate galaxy growth (Davé et al. 2011), and there is some evidence that metal-rich outflows can travel large distances from at least some galaxies (e.g., Tripp et al. 2011).

Thus, it is important to understand the impact of large-scale inflows and outflows to obtain a complete picture of how galaxies form and evolve. However, observationally tracking the galactic inflows and outflows comprising important portions of the “baryon cycle” can be observationally challenging – gases flowing through the circumgalactic medium (CGM) will often have low densities, and their emission features are expected to be faint and difficult to detect. Consequently, absorption spectroscopy, which is much more sensitive to low-density gas, has become the workhorse method for observing the baryon cycle and the CGM. Intervening damped and sub-damped Ly α absorbers (DLAs) with $N(\text{H I}) \gtrsim 10^{19} \text{ cm}^{-2}$, detected in the spectra of background quasi-stellar objects (QSOs), can be particularly interesting because they exhibit absorption in a wide array of elements and ionization stages (Péroux et al. 2003; Prochaska et al. 2003; Wolfe et al. 2005) and thereby enable detailed studies of abundances and physical conditions. From $z = 0$ to $z \gtrsim 5$, gas-phase abundances in DLAs and sub-DLAs decrease with increasing redshift, but the scatter is large in all redshift bins (≈ 1 dex), presumably reflecting the different histories of

the absorbing gas (Kulkarni et al. 2007; Meiring et al. 2009; Rafelski et al. 2012).

To maximize the use of QSO absorbers for the study of galaxy evolution, it is necessary to understand the relationships between the absorption systems and the galaxies/environment. In this regard, DLAs have been curiously difficult to pin down, and they can arise in difficult-to-study objects such as low surface-brightness galaxies and galaxies with very low star-formation rates (e.g., Bowen et al. 2001; Tripp et al. 2005; Battisti et al. 2012; Fumagalli et al. 2015). Low-redshift absorbers are advantageous for probing absorber-galaxy relationships because their environments can be investigated with exceptionally deep imaging and spectroscopy, and methods such as 21 cm emission mapping can be applied (e.g., Rosenberg et al. 2006; Borthakur et al. 2011, 2014, 2015; Chengalur et al. 2015; Burchett et al. 2016; Péroux et al. 2017; Kanekar et al. 2018). Such studies have demonstrated that absorbers in galaxy group environments are relatively common (Bielby et al. 2017; Péroux et al. 2017; Borthakur et al. 2018; Klitsch et al. 2018) but there is also evidence that the CGM is removed (or is highly ionized) in some high-density environments (Johnson et al. 2014; Burchett et al. 2016, 2018).

One such low-redshift absorber is the low- z sub-DLA at $z \simeq 0.075$ in the spectrum of the PG 1543+489 ($z_e = 0.40$). This absorption system has some puzzling characteristics and warrants follow-up observations for several reasons. Two intervening galaxies also at $z = 0.075$ originally identified close to the QSO sightline (Monk et al. 1986) have relatively large impact parameters ρ of 64 and 119 kpc, but surprisingly the first absorption lines detected at the redshifts of these galaxies were the optical Ca II H & K lines (Bowen et al. 1991). With an ionization potential of only 11.87 eV, Ca II is easily photoionized in many contexts, and the detection of Ca II H & K absorption usually implies a significant column density of H I in the absorption system (Wild et al. 2007; Zych et al. 2007; Nestor et al. 2008). However, high $N(\text{H I})$ values are not expected at large galactocentric distances, so the detection of Ca II was intriguing. Follow-up ultraviolet (UV) observations with the Goddard High Resolution Spectrograph (GHRS; Brandt et al. 1994) on the *Hubble Space Telescope* (HST) by Bowen et al. (1995) targeted the Mg II $\lambda\lambda 2796, 2803$ absorption doublet. These lines were successfully detected, had moderately strong equivalent widths, and exhibited simple component structure. At the time, Bowen et al. suggested that the Ca II and Mg II absorption might arise in tidal debris lying between the two nearby galaxies, or that a much fainter dwarf galaxy lay hidden directly along the sightline, obscured by the glare of the background QSO. They also considered that the absorption might be related to the disk of the nearest, highly inclined galaxy, because the projection of its disk along the major axis aligns closely with the position of the QSO sightline — even though the H I in the disk was not expected to extend out to 64 kpc at the levels of $N(\text{H I})$ suggested by the metal-line absorption. Since these results were published, research into the CGM of galaxies has advanced other possible origins for ab-

sorption lines, such as warm outflows arising from bursts of star formation (or AGN) activity (e.g., Strickland et al. 2004; Weiner et al. 2009; Rupke & Veilleux 2011; Tripp et al. 2011; Chisholm et al. 2015; Muzahid et al. 2015), cold flows from the IGM (Kereš et al. 2005; Dekel et al. 2009; Ribaldo et al. 2011; Bouché et al. 2013; Rahmani et al. 2018), or large gas disks that may be corotating with the stellar disks of galaxies (Steidel et al. 2002; Ho et al. 2017).

In this study, we present new spectroscopic observations of the absorption system toward PG 1543+489 with HST and additional ground-based observations of objects in the field of PG 1543+489. The HST spectra were acquired with the Space Telescope Imaging Spectrograph (STIS), and were designed to measure the metallicity and ionization structure of the absorbing gas, while the optical data were obtained to better understand its origin. In addition, PG 1543+489 itself is an interesting object, being one of the most luminous ($M_B = -26$) radio-quiet narrow line QSOs in the low-redshift universe (Schmidt & Green 1983) with a gas outflow that extends 1150 km s^{-1} from the systemic redshift of the QSO (Aoki et al. 2005). Some of our data may provide insight on the nature of the QSO, although in this paper we focus on the foreground absorption system noted above.

This paper is organized as follows: in §2 we present a synopsis of the available information on the galaxies in the field of PG 1543+489, and present new ground-based imaging and spectroscopic data of the galaxies. In §3 we show the HST STIS spectra of PG 1543+489 and new absorption lines from the intervening absorption system. §4 discusses the abundances of the absorbing gas derived from the new HST data and the ionization models required to better constrain the abundances. Finally, in §5 we summarize our results and discuss their implications. Throughout the paper, we adopt a cosmology with $H_0 = 70 \text{ km s}^{-1} \text{ Mpc}^{-1}$, $\Omega_M = 0.3$, and $\Omega_\Lambda = 0.7$.

2. GROUND-BASED OBSERVATIONS OF THE PG 1543+489 FIELD

The field around PG 1543+489 is covered by the Sloan Digital Sky Survey (SDSS), which provides some relevant spectroscopic galaxy redshifts as well as accurate broadband magnitudes. To investigate the connections between the absorption system at $z = 0.075$ and nearby galaxies, we make use of information from SDSS Data Release 14 (DR14) as well as our own spectroscopic observations of galaxies in the PG 1543+489 field. Prior to SDSS spectroscopic observations of this field, in 2002 June we collected spectroscopic redshifts of galaxies near the QSO sightline using the Dual Imaging Spectrograph (DIS) on the Apache Point Observatory (APO) 3.5m telescope. We used a 1.5 arcsec slit with the B300 and R300 gratings to cover a wavelength range of $\sim 3400 - 7700 \text{ \AA}$, and we measured the redshifts of galaxies from their emission lines. Later, some of these galaxies were also observed as part of the SDSS spectroscopic galaxy survey (Strauss et al. 2002). Information on galaxies from our APO program that we use in this paper (in addition to the SDSS DR14 data) is provided in Table 1, including spectro-

Table 1. Galaxies in the Field of PG 1543+489

SDSS	APO		r	M_r	L_{gal}	M_r^*	ρ	ρ
ID	ID	z_{gal}	(mag)	mag	(L^*)	($\log[M_\odot]$)	($''$)	(kpc)
(1)	(2)	(3)	(4)	(5)	(6)	(7)	(8)	(9)
J154527.12+484642.2	G1	0.0751	16.7	-20.9	2.0	10.5	0.76	64
J154534.68+484702.3	G86	0.0754	19.0	-18.7	0.3	9.7	1.15	98
J154526.59+484453.8	G2	0.0753	16.0	-21.7	4.0	10.8	1.39	119
J154533.92+484754.1	G96	0.0750	19.9	-17.7	0.1	9.3	1.85	158
J154528.52+484759.4	G142	0.0759	17.9	-19.7	0.7	10.1	1.86	160
J154534.48+484814.0	...	0.0	17.4	2.20	...
J154535.86+484814.0	G74	0.0968	18.3	-19.9	0.8	10.1	2.28	245
J154519.31+484808.9	G221	0.1536	18.1	-21.2	2.6	10.6	2.69	430

NOTE—Columns: (1) SDSS ID from SDSS DR14; (2) galaxy name adopted in this paper based on the nomenclature of the APO survey in 2002; (3) galaxy redshift. For the first three galaxies, G1, G86, and G2, DR14 redshifts are listed. The rest were measured at APO. (4) Galaxy de-reddened r -band magnitude of the galaxy from DR14; (5) absolute r -band magnitude; (6) galaxy luminosity assuming $M_r^* = -21.2$ at $z = 0.1$, from Bell et al. (2003); (7) stellar mass assuming color corrections from López-Sanjuan et al. (2018); (8) and (9) impact parameter of galaxy from QSO sightline, in arcsec and (proper) kpc. N.B. This table lists all the galaxies with known redshifts in the group at $z \simeq 0.075$ within 200 kpc of the QSO sightline.

scopic redshifts, SDSS r -band magnitudes, angular and physical separations of the galaxies from the QSO sightline, and estimates of the luminosities and stellar masses of the galaxies.

We also obtained broadband images of the QSO field with SPICAM on the APO 3.5m telescope in the R - (50 minutes total exposure), g - (80 minutes) and i -bands (93 minutes) in 2002 and 2003. Figure 1 shows a false-color composite image constructed by combining the SPICAM data from the three bands. This image is deeper than the SDSS images in similar passbands and reveals some important morphological details that cannot be discerned in SDSS images (see below). Nevertheless, the photometric calibration of the SDSS data is better, so when available, we prefer SDSS photometry for the well-detected bright galaxies that are relevant to this study.

2.1. The galaxy group affiliated with the PG 1543+489 sub-DLA

The brightest foreground galaxies lying near the sightline toward PG 1543+489 are at impact parameters $\rho = 64$ and 119 kpc. The SDSS designations for both are listed in Table 1, but in the rest of this paper, we refer to the two as “G1” and “G2,” in keeping with their original designations by Monk et al. (1986). Our APO survey has revealed a third — albeit fainter — galaxy with a redshift similar to those of G1 and G2 and a comparable impact parameter of $\rho = 98$ kpc (G86; see Table 1). In addition, the APO survey located two other galaxies at similar redshifts with $\rho = 158$ and 160 kpc

(G96 and G142 in Table 1). Thus, a group of five galaxies, all within an impact parameter of 160 kpc from the sightline, is found at the absorber redshift. These galaxies are identified with red labels in Figure 1. Objects with spectroscopic redshifts that are significantly different from the group redshift are also indicated in Figure 1 with white or blue labels.

SDSS provides additional information on galaxies at angular separations from the sightline larger than the angular limit of our APO survey. To investigate the larger scale extent of the group at $z = 0.075$, we collated all galaxy redshifts available from SDSS DR14 within a radius of 122 arcmin, or 10 Mpc at the group’s redshift. As our sample was drawn from SDSS, we have a similar limiting magnitude of $r \simeq 17.8$, or $M_r = -19.9$ (i.e., $0.1 L_r^*$, at $z = 0.075$), although some of the galaxies observed at APO are fainter than this limit. The two-dimensional distribution of the galaxies within the range $20,000 \leq cz \leq 24,000$ displays no clear large-scale structural features (e.g., galaxy filaments) or any association with, e.g., a denser cluster, but a group of galaxies appears to be confined to a radius of $\approx 0.6^\circ$, or 3.1 Mpc, around the QSO sightline, at the group redshift of ~ 0.075 . The one-dimensional distribution of these galaxies is shown in Figure 2. The peak of the distribution occurs at $22,710 \pm 30 \text{ km s}^{-1}$, with the three galaxies G1, G86, and G2 all offset to slightly lower velocities (see the red vertical lines in Figure 2). The group consists of 21 galaxies within $\pm 500 \text{ km s}^{-1}$ of $z = 0.075$, and apart from G1 and G2, only

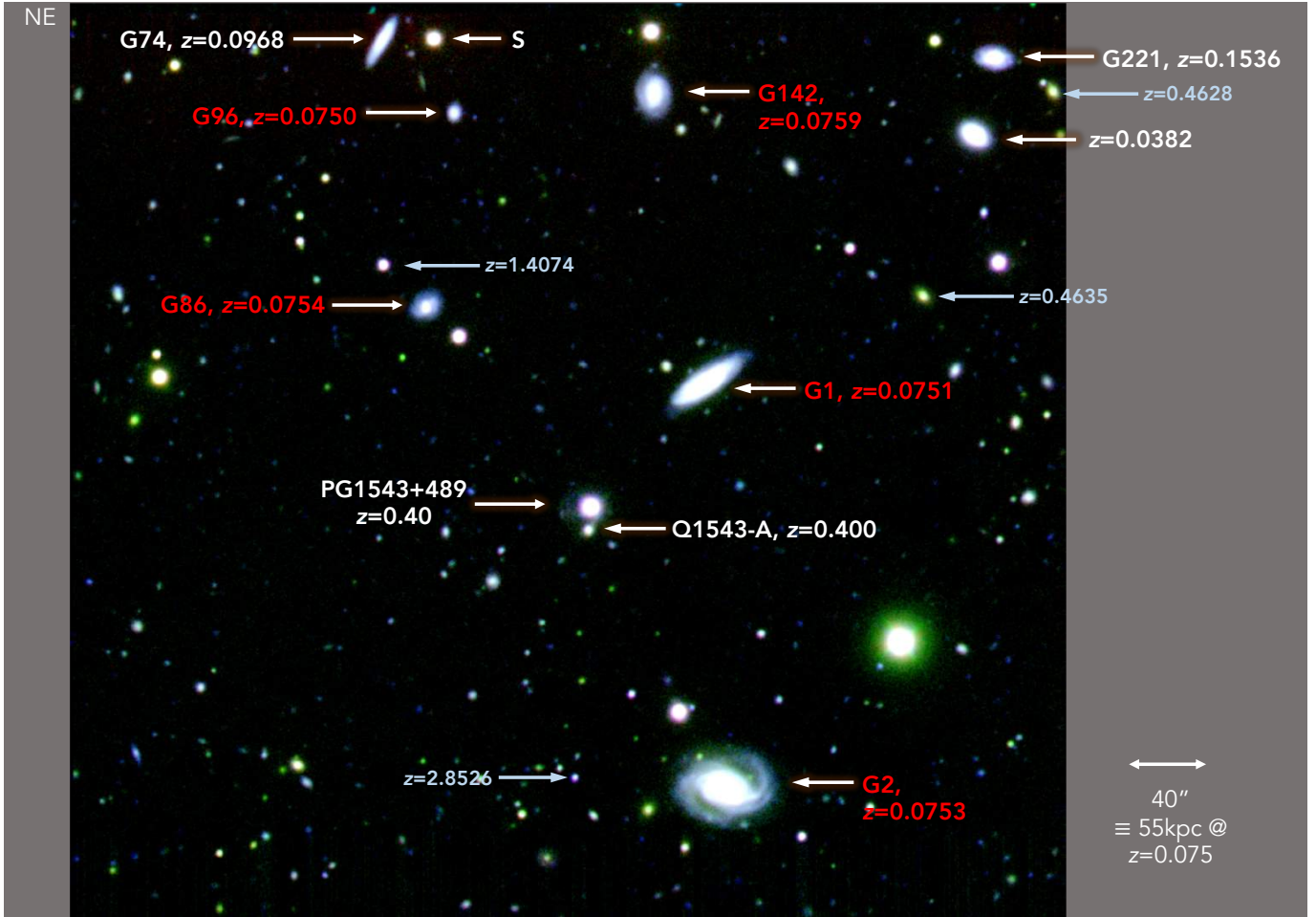


Figure 1. False-color image of the field of PG 1543+489 using g -, R -, and i -band images taken with the APO 3.5m telescope. All objects with known spectroscopic redshifts, either from DR14 or our APO spectroscopic observations, are labeled. The background QSO at $z = 0.40$ is shown, as well as the five galaxies at $z \simeq 0.075$ lying within an impact parameter of $\simeq 200$ kpc from the QSO sightline (labeled in red) and one star ('S'). Objects that are at or in front of the QSO but are otherwise not relevant to this study (because the objects are at significantly different redshifts from the absorption-line system) are annotated with white labels, and small blue labels mark objects that are behind the QSO at higher redshifts. The field of view is 7.2×5.3 arcmin.

two other galaxies are obviously disks, with the rest being of early or S0 type. It is possible that G1 and G2 are therefore in their early stages of falling into a rich group of galaxies.

2.2. Properties of G1

In order to obtain spatially resolved information on G1 (e.g., its rotation curve), we again used DIS at APO, this time with a 1.5 arcsec slit aligned along the major axis of the galaxy. The data were taken on 2005 March 11 with the B300/R300 gratings, and we obtained five 1200 s exposures at high air-mass. The spectra were binned on-chip to give a spatial dispersion of 0.84 arcsec pix^{-1} , and a spectral resolution of 300 km s^{-1} FWHM. The five individual frames were debiased, flat-fielded, and then coadded to produce a final 2D frame. Each row (spectrum) was wavelength-calibrated using the same row from an arc lamp exposure taken prior to the start of the observations. Finally, the data were flux-calibrated using the standard star BD+33d2642.

2.2.1. Metallicity and star-formation rate of G1

Emission lines of [O II] $\lambda 3727$, [O III] $\lambda \lambda 4959, 5007$, $H\beta$, $H\alpha$, and [N II] $\lambda 6583$ were detected from many of the individual CCD rows comprising the galaxy spectrum. The total $H\alpha$ flux from G1 summed over all these rows is $\simeq 1.0(\pm 0.2) \times 10^{-14}$ ergs cm^{-2} s^{-1} . This includes all the flux from the disk of the galaxy, but does not account for losses from the galaxy being slightly wider than the slit or from internal extinction, which we cannot measure due to the non-detection of other Balmer lines. $H\alpha$ decreases as galactocentric distance r increases and is depressed in the inner 2.5–4.2 arcsec, unlike [N II] which shows no such dip at small r .

The $H\alpha$ and the [N II] lines enable us to measure the gas-phase metallicity of G1 using the strong-line N2 index, defined as $N2 = \log([\text{N II}] \lambda 6583 / H\alpha)$. N2 is largely constant across the disk except in the inner region where $H\alpha$ decreases. This may indicate a change in ionization by a non star-forming source, such as a low-luminosity AGN at the

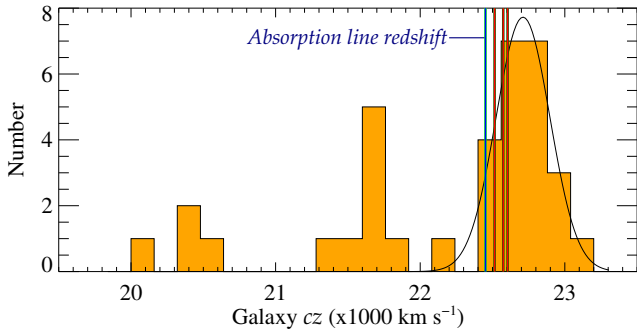


Figure 2. Redshift distribution of galaxies from DR14 and our own redshift survey within 0.6° of the sightline to PG 1543+489, or ≈ 3.1 Mpc. The absorption-line redshift at $z = 0.07489$ is indicated by the blue vertical line, while the redshifts of the three central galaxies are marked with red vertical lines (from left to right, G1, G2, and G86). A Gaussian fit to the profile gives the center of the distribution to be $22,710 \pm 30$ km s $^{-1}$, with a width of $\sigma \sim 190 \pm 30$ km s $^{-1}$. Although not shown in this figure, these galaxies are spread roughly uniformly in two dimensions within the 0.6° radius.

galaxy’s center. If we ignore this region, then the lower limit to the $H\alpha$ flux is $7.5 (\pm 0.3) \times 10^{-15}$ ergs cm $^{-2}$ s $^{-1}$. The resulting total $H\alpha$ luminosity is $\log[H\alpha \text{ (ergs s}^{-1})] = 41.02 \pm 0.01$, which gives a star formation rate of $0.8 \pm 0.03 M_\odot \text{ yr}^{-1}$ using the relationship given by Kennicutt (1998).

The average N2 ratio for the two outer regions is similar, -0.32 ± 0.04 , which gives a metallicity of $\simeq 8.60 \pm 0.02$ using the calibration of Marino et al. (2013),¹ or $[O/H] = -0.10 \pm 0.05$, i.e. ~ 0.8 times the solar value assuming $12 + \log[O/H]_\odot = 8.69 \pm 0.05$ (Asplund et al. 2009). We note that this is only 0.1 dex smaller than that derived using the original N2 calibration of Pettini & Pagel (2004), whose sample was more sparse than the data available to Marino et al. (2013). The measurement errors on N2 for individual spatial pixels are larger, $\approx \pm 0.1$ dex, and there is no compelling evidence for a change in N2 as a function of galactocentric radius — as might be expected from a metallicity gradient in the disk — given the large errors. We return to this measurement in §5.

2.2.2. Rotation curve of G1

Having extracted 1D spectra from individual CCD rows of our APO data, and with the slit oriented along the major axis of G1, we were able to construct a rotation curve of the galaxy from the emission lines (Figure 3). The seeing at the time was 1–2 arcsec FWHM, so each row of the

¹ As is customary for interpreting metallicity measurements based on the analysis of emission lines, we note that electron-temperature-based empirical calibrations produce metallicities that are ~ 0.2 – 0.4 dex lower than strong-line methods based on photoionization models, such as the N2 index used herein (e.g. Kewley & Ellison 2008; López-Sánchez et al. 2012, and references therein).

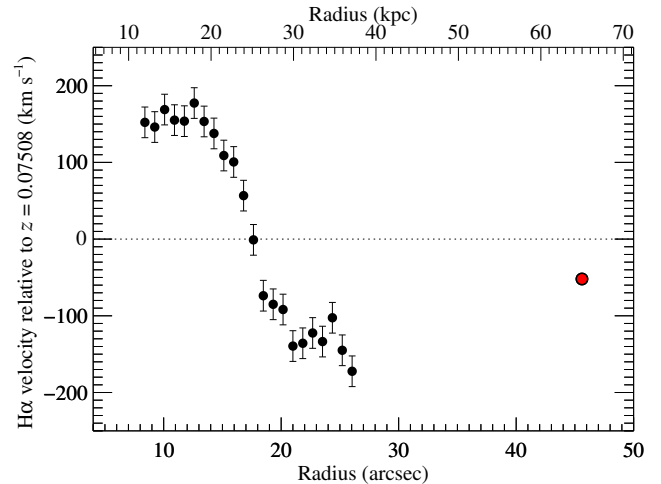


Figure 3. The rotation curve for galaxy G1 toward PG 1543+489, determined from $H\alpha$ emission lines (black points). The velocity of the absorption system at $z = 0.07489$ fit to the H I Ly α line is shown as a red circle.

CCD (0.83 arcsec pix $^{-1}$) corresponds to a sampling of approximately half a resolution element. We measured the velocity in two ways, first by fitting Gaussian profiles to the $H\alpha$ and [N II] lines, and then by using the FXCOR routine in IRAF, which computes radial velocities between spectra via Fourier cross-correlation. With the latter method, we used the 1D spectrum at the center of the galaxy as the reference spectrum. Both methods gave similar results, to within the errors generated by the FXCOR routine. We return to the relationship between the velocity of the disk and the absorption detected toward PG 1543+489 in §5.

2.3. A search for faint galaxies close to the sightline of PG 1543+489

With our prior knowledge of the peculiar nature of the absorption system toward PG 1543+489, we were motivated to search for other faint galaxies close to the sightline that could be the source of the absorption rather than the three galaxies close to the sightline listed in Table 1. A closer and more detailed representation of the APO composite image of the QSO field is shown in Figure 4. Apart from the bright satellite galaxy to the south of the QSO (labeled Q1543–A), which is known to be at the redshift of PG 1543+489 (Bowen et al. 1995), there is additional nebulousity directly to the east of the QSO. In this section, we discuss data which we obtained in order to measure the redshift of this ‘fuzz.’ In principle, this fuzz could be the hypothesized galaxy close to the sightline that is the source of the absorption-line system, but the host galaxies of QSOs are often readily apparent in images of this depth, so this could, alternatively, simply be light from the QSO host galaxy. As we show below, all available evidence indicates that the fuzz is indeed the host galaxy of the QSO and is unrelated to the absorption system.

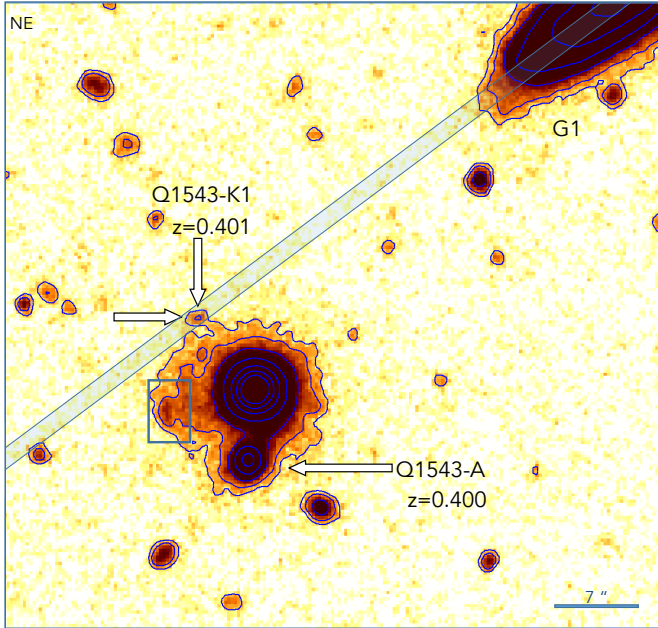


Figure 4. Image of the QSO PG1543+489, which has a redshift of $z = 0.401$. This figure shows the g -, R - and i -band images added together to improve the signal-to-noise ratio of low surface brightness features. The sightline to the QSO passes through the CGM of galaxy G1. A small satellite, labeled Q1543-A, has the same redshift as PG 1543+489 (Bowen et al. 1995) and lies $6''.0$ or 32 kpc, away on the plane of the sky. Interestingly, a combination of clumpy and diffuse emission is seen around the QSO out to large radii of $\sim 8''$ toward the east. We have measured a redshift of $z = 0.40$ for one particular clump, at a separation of $7''.3$ or 40 kpc, labeled here as Q1543-K1. The DIS slit used to measure the rotation curve of G1 and detect the emission from K1 is shown in blue. The blue box shows the field of view of our GMOS-N IFU observations. The orientation is the same as in Figure 1.

Fortuitously, the orientation of the DIS slit used to measure the rotation curve of G1 also passed through a bright knot in the extended fuzz surrounding the QSO, which we label as Q1543-K1 in Figure 4. Q1543-K1 has a g -band magnitude of 24.2 ± 0.9 and lies 7.3 arcsec from the QSO sightline. At the position of Q1543-K1, our APO spectrum shows clear emission lines of $H\alpha$, $[O\ III] \lambda\lambda 4959, 5007$, $H\beta$, and $[O\ II] \lambda 3727$ at a redshift of 0.401, i.e., the same as the QSO redshift and satellite Q1543-A.

In addition to the APO data, we used the Gemini Multi-Object Spectrograph North (GMOS-N) IFU unit in the optical to search for emission lines at the redshift of the QSO or that of the absorption-line system. We acquired nine 1200 s integrations in June and July 2016 centered on the most easternmost part of the fuzz, with a 3.5×5 arcsec field of view shown as a blue box in Figure 4. Our observations used the grating to give a central wavelength of 7000 \AA and a coverage of $5618 - 6922 \text{ \AA}$ at a measured dispersion of $0.47 \text{ \AA pix}^{-1}$. In this observing mode, the data read out into an array

of 33×49 spatial pixels (spaxels) for each wavelength interval. We reduced the data using the IRAF/Gemini software pipeline, with the addition of the LACOSMIC task which ensures a robust removal of cosmic rays (van Dokkum 2001). The IRAF/Gemini set of tasks does not include a means to coadd multiple 3D data cubes (in our case, nine separate integrations), so we created a separate module for that task.

The final coadded data cube showed no evidence for any emission lines from the QSO or from the intervening absorption-line system. Binning the data spatially by up to a factor of 8 failed to show any signal. We note that the only grating option available at the time of the observations was R400, which covers only the $H\beta$ emission line at the redshift of the QSO, and no emission lines at the redshift of G1. The non-detection of $H\beta$ is unfortunate, and also not so surprising, as the $H\beta$ emission line is already established to be weak in our spectrum of the Q1543-K1 fuzz component.

The presence of a well-detected companion (Q1543-A) to the south of the QSO suggests that these two objects could be interacting. Such interactions often produce extended nebulosity similar to the ‘fuzz’ in Figure 4, and because the brightest spot in the fuzz has the same redshift as the QSO, it is most likely that the fuzz is due to material in the immediate vicinity of PG 1543+489 and is not a foreground galaxy affiliated with the absorption-line system.

3. HIGH-RESOLUTION ULTRAVIOLET SPECTROSCOPY OF PG 1543+489

To expand on our set of the Ca II H & K and Mg II $\lambda\lambda 2796, 2803$ ions for analysis of the absorption-line system, we reobserved PG 1543+489 with STIS on 13 October 2001 using the G140M grating and the $52'' \times 0''.1$ aperture. This STIS grating has a spectral resolving power $R \approx 10000$, i.e., spectral resolution $\approx 30 \text{ km s}^{-1}$ (Woodgate et al. 1998). Two wavelength settings were used, with central wavelengths of 1272 and 1321 \AA , for a total exposure of 189 minutes. After applying the standard CALSTIS pipeline to extract the one-dimensional spectra, we coadded the overlapping regions of the two spectra with a weighting based on the inverse of each spectrum’s variance. This produced a single spectrum covering the 1245 – 1349 \AA wavelength range.

Several resonance transitions of important species at the redshift of the absorption-line system are covered in this observed spectrum, including the H I Ly α line; the N I $\lambda\lambda 1199.55, 1200.22$ and 1200.71 triplet; Si II $\lambda\lambda 1190.42, 1193.29$; Si III $\lambda 1206.50$, N V $\lambda\lambda 1238.82, 1242.80$; and two of the three lines of the S II triplet at 1250.58 and 1253.81 \AA . Of these target lines, the new STIS spectrum clearly revealed the H I Ly α , N I, Si II, and Si III lines at high significance. The S II and N V features are not apparent above the noise in the new data. We note that low-resolution spectra of PG 1543+489 have also been recorded with the Faint Object Spectrograph and the Cosmic Origins Spectrograph (e.g., Borthakur et al. 2013). Unfortunately, due to the low spectral resolution, these additional data are much less sensitive and generally do not place sufficiently stringent limits on metal absorption lines to be useful for the purposes of this paper.

Table 2. Column densities of ions and element ratios at $z=0.07489$ toward PG1543+489

	Component 1	Component 2
	$v = 2.2 \pm 1.0 \text{ km s}^{-1}$	$v = 12.2 \pm 0.9 \text{ km s}^{-1}$
	$b = 10.2 \pm 1.8 \text{ km s}^{-1}$	$b = 31.6 \pm 1.6 \text{ km s}^{-1}$
$\log N(\text{H I})$	19.08 (± 0.05) ^a	–
$\log N(\text{N I})$	13.91 (–0.05, +0.07)	$\lesssim 13.0$
$\log N(\text{N V})$	< 13.5	< 13.5
$\log N(\text{N I/H I})$	–5.17 (–0.07, +0.09)	–
$Z(\text{N/H})$ ^b	–1.0 (± 0.1)	–
$\log N(\text{Si II})$	13.72 (–0.08, +0.22)	13.69 (–0.07, +0.03)
$\log N(\text{Si III})$	13.10 (± 0.29)	13.53 (–0.04, +0.02)
$\log N(\text{Si II+Si III})$	13.81 (–0.09, +0.19)	–
$Z(\text{Si/H})$ ^b	–0.78 (–0.11, +0.20)	–
$\log N(\text{Mg II})$	13.40 (–0.19, +0.36)	13.31 (–0.09, +0.06)
$\log(\text{Mg II/H I})$	–5.68 (–0.20, +0.36)	–
$Z(\text{Mg/H})$ ^b	–1.25 (–0.20, +0.37)	–
$\log N(\text{S II})$	< 14.5	< 14.5

^aThe units of all column density values are in cm^{-2} .

^bThese are the abundances $Z = \log[X/\text{H}] - \log[X/\text{H}]_{\odot}$ that N, Si, and Mg would have if there were no ionization corrections and no dust depletion in the absorber for component 1. Solar values are $\log N$: 7.83 \pm 0.05; Si: 7.51 \pm 0.03, and Mg: 7.57 \pm 0.04, from [Asplund et al. \(2009\)](#).

We continuum-normalized the STIS data using the methods outlined by [Sembach & Savage \(1992\)](#) (see below), and show the normalized absorption profiles of the detected lines in Figures 5 and 6. We also reanalyzed the Mg II lines observed with GHRS by [Bowen et al. \(1995\)](#), using the archival data but reprocessed with the final version of the CALHRS pipeline, v1.3.14 (2004), which includes several iterations of pipeline improvements implemented after the calibration of the data shown in the original paper. The re-reduced and continuum-normalized Mg II profiles are also shown in Figure 6.

As expected, the H I Ly α line shows strong damping wings (see Figure 5), and these wings provide excellent constraints on the total H I column density of the absorber. By the fitting the H I Ly α line with a single damped profile, we obtain $z_{\text{abs}} = 0.07489$, which we adopt for the systemic redshift of the absorption system. We also obtain a total column density (in cm^{-2}) of $\log N(\text{H I}) = 19.08 \pm 0.05$. This result shows that the absorption-line system falls into the category of the sub-DLAs introduced in §1. However, as we discuss below, the absorption profiles of the metals show clear indications of two absorption components, which introduces a complication in our analysis of the absorber ionization and metallicity;

although the damped Ly α profile provides a precise measurement of $N(\text{H I})$, this is the total column density summed over both components. Consequently, we will need to consider how the H I might be distributed between the two components in our ionization modeling.

To derive the velocity centroids (v), column densities (N), and Doppler parameters (b) of the metal absorption lines shown in Figure 6, we fitted Voigt profile models, convolved with the STIS line-spread function for the G140M grating, to the normalized data. We fitted all eight metal lines simultaneously, allowing the individual metal column densities N to vary but requiring that all metals in a given component have the same v and b values². We found that while a single-component fit was adequate for the N I triplet, it could not reproduce the structure seen in the Si II, Si III, or Mg II lines, which clearly exhibit an additional weaker (but blended) component redward of the stronger one. Our best-fit Voigt-profile models are overlaid on the data in Figure 6, and the profile parameters are summarized in Table 2. In Figure 6, we show the full fit (i.e., including both components) to each profile with a solid blue line, but we also show the models for the two discrete components with red solid lines. In one instance (the Si III line), it was necessary also to model the contribution from an H I Ly δ line at a different redshift ($z_{\text{abs}} = 0.36583$) that is moderately blended with the Si III absorption. Fortunately, the shape of this blended interloper is tightly constrained because H I Ly ϵ , Ly ζ , and Ly η at the same redshift are covered by the STIS data. Consequently, this blend has little impact on our Si III measurements. For the metal lines, uncertainties in the profile parameters were estimated using the method of [Bowen et al. \(1995\)](#). The error that we report for the H I column was derived by considering the upper and lower bounds on the continuum from the formalism of [Sembach & Savage \(1992\)](#), as implemented by [Bowen et al. \(2008\)](#).

We corroborate the two-component structure that we inferred from Voigt-profile fitting by performing an independent apparent column density analysis ([Savage & Sembach 1991](#)) of the Si II $\lambda 1190, 1993$ lines. This approach can also be used to reveal unresolved saturation in components if multiple transitions with different oscillator strengths are available. The apparent column density profiles for the Si II lines are shown in Figure 7, where it is clear that the values for the apparent optical depth $N_a(v)$ of the two lines do not match, indicating the presence of unresolved saturation in one or both of the lines. As the saturation is expected to be only moderate, it can be corrected using the prescription given by [Jenkins \(1996\)](#). The result of such a correction is shown as a black line in Figure 7, and we see that two components are indicated by direct analysis of the apparent column density profiles. We also find that integration of the saturation-corrected apparent column density profile yields a total column density

² The constraint of a fixed b -value for all of the metals implicitly assumes that the line widths are dominated by microturbulence within the absorber rather than by thermal broadening.

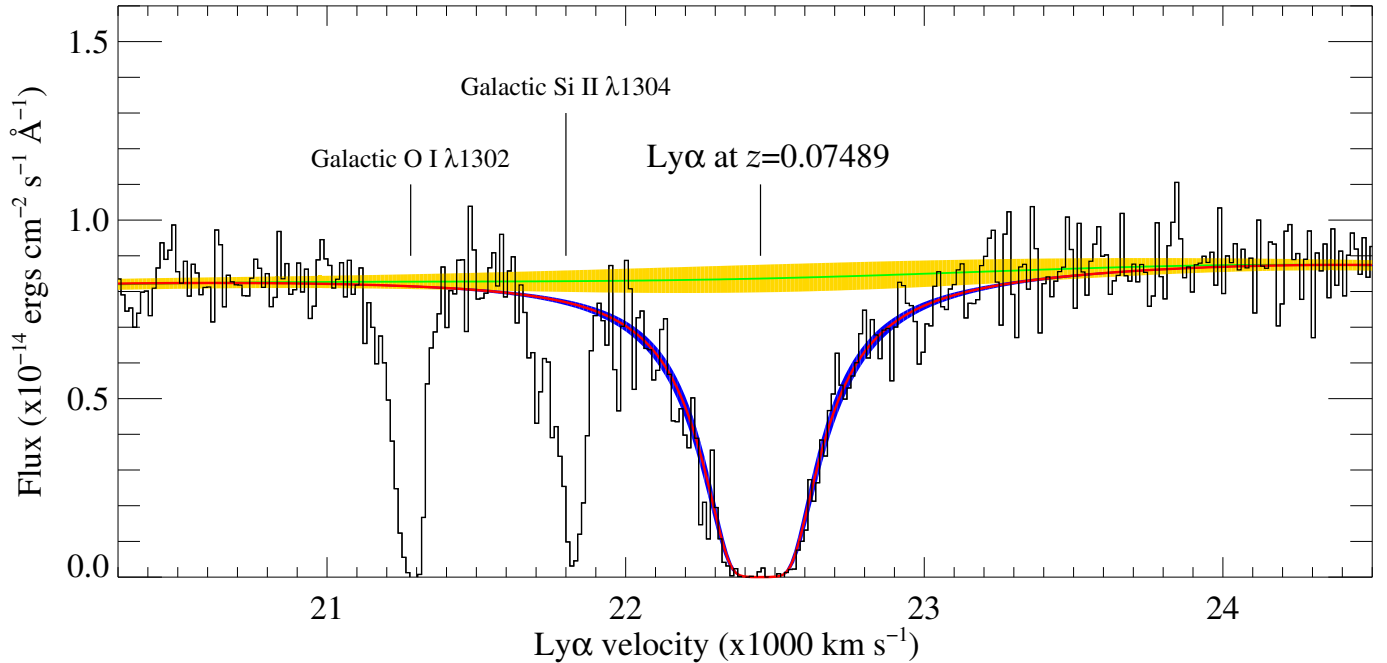


Figure 5. Portion of the STIS spectrum of PG 1543+489 showing strong Ly α absorption at $z = 0.07489$. The fit to the continuum is shown as a green line, while the range bounded by the upper and lower continuum fits used to derive the error in $N(\text{H I})$ is shown in yellow. The best Voigt profile fit to the Ly α line is drawn in red, while the region bounded by $\pm 1\sigma$ differences in $N(\text{H I})$ is shown in blue.

in good agreement with our profile fitting results. The same saturation is also seen in the profile fits to the Mg II lines, a result we return to in the next section.

For convenience, we hereafter refer to the two components as “component 1” and “component 2” as labeled in Table 2.

4. IONIZATION MODELS AND ABSORBER ABUNDANCES

We now examine the implications of the new STIS measurements regarding the abundances of the sub-DLA of PG 1543+489, which can provide insight into the origin and history of the absorbing gas. As noted above, measurement of chemical abundances in this system is somewhat complicated by our conclusion that there are two components in the metal absorption profiles (see previous section), while we only have constraints on the total H I column. To overcome this problem, we have conducted two analyses of the absorber abundances.

We consider the total N I and H I column densities to estimate the overall metallicity summed over both components. In gas that is not severely ionized, N I is tied to H I by charge exchange (Butler & Dalgarno 1979), so even if the gas is somewhat affected by photoionization by UV background light (as one might expect given the apparent location of the absorber in the CGM), ionization corrections can be ignored for these two species. If we assume that ionization corrections can be ignored for N I, we obtain

$$\left[\frac{\text{N}}{\text{H}}\right] = \log\left(\frac{N(\text{N I})}{N(\text{H I})}\right) - \log\left(\frac{\text{N}}{\text{H}}\right)_{\odot} = -1.0 \pm 0.1 \quad (1)$$

where $(\text{N}/\text{H})_{\odot} = -7.83 \pm 0.05$ is the solar nitrogen abundance.

It is well known that in various contexts, nitrogen can be less abundant than other elements, particularly α -capture elements, compared to solar relative abundances due to its complex nucleosynthetic origins (e.g., Vila Costas & Edmunds 1993; Pettini et al. 2008; Battisti et al. 2012, and references therein), so this [N/H] measurement might underrepresent the overall level of enrichment of the sub-DLA. Therefore, we are motivated to investigate the abundances implied by the Si II, Mg II, and Si III lines as well. Unlike the case for nitrogen, the corrections for these other species could be important. For example, in addition to Si II being in the same gas phase as the H I, some of the Si II could also arise in more highly ionized gas that does not contribute significantly to the measured H I column density. Indeed, the detection of Si III absorption indicates the presence of some significantly ionized material somewhere in the absorption system.

For these reasons, we have also investigated how ionization corrections could alter the derived abundances. In general, the logarithmic gas-phase abundance of ion X^i with respect to hydrogen is

$$\left[\frac{X^i}{\text{H}}\right] = \log\left(\frac{N(X^i)}{N(\text{H I})}\right) - \log\left(\frac{X}{\text{H}}\right)_{\odot} + \log\left(\frac{f(\text{H I})}{f(X^i)}\right), \quad (2)$$

where N is the column density, f is the ion fraction, $[X/\text{H}]_{\odot}$ is the solar abundance of element X with respect to H, and i is the ionic species; the last term in equation 2 is the ionization correction. We use the photoionization code CLOUDY (version 13.03, Ferland et al. 2013) to model the ionization of the gas. Given the H I column density of the

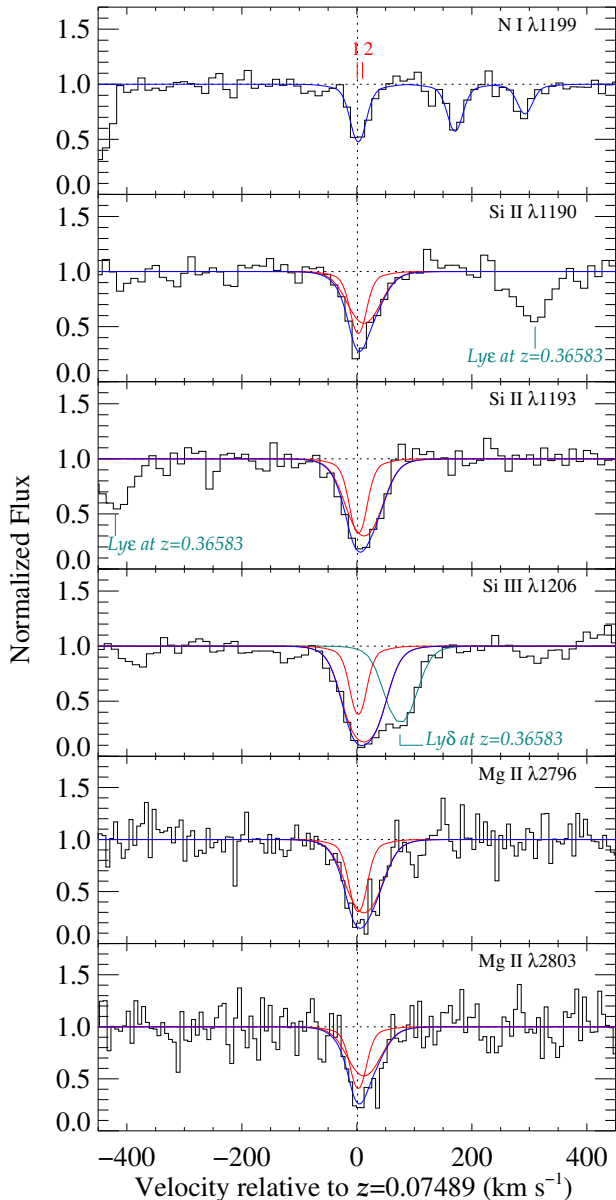


Figure 6. Velocity plot of the STIS and GHRS (the latter covering the Mg II lines) spectra of PG 1543+489, showing the lines detected at $z = 0.07489$. For N I, the spectrum is centered on the $\lambda 1199.5$ line, but the fits to the $\lambda 1200.2$ and $\lambda 1200.7$ lines are also shown at higher velocity. The Si III $\lambda 1206$ line is blended with an Ly δ line at $z = 0.3658$, but that line can be modeled (shown in teal) by fitting Ly γ , Ly ϵ , Ly ζ , and Ly η lines ($\log N(\text{H I}) = 15.37 \pm 0.02$, $b = 27.8 \pm 1.2 \text{ km s}^{-1}$) detected elsewhere in the data. The two components of the best-fit model are shown as red lines, and their resulting composite as a blue line.

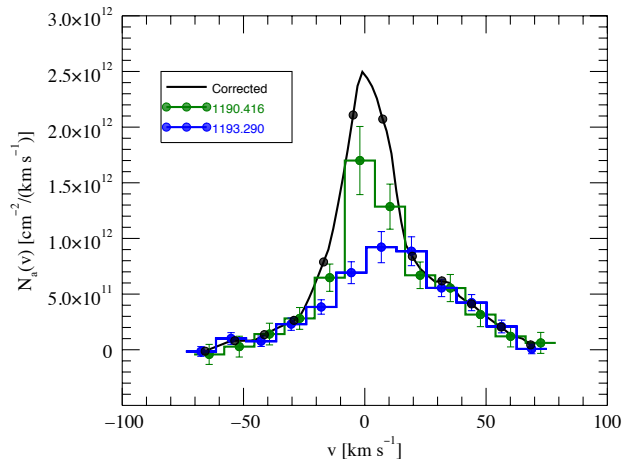


Figure 7. The apparent column densities of the Si II $\lambda\lambda 1190, 1193$ lines in the sub-damped Ly α absorber at $z_{\text{abs}} = 0.07489$ in the spectrum of PG 1543+489. The peaks of each line do not match in height, indicating the presence of some unresolved saturation. The corrected apparent column density, derived using the technique of Jenkins (1996), indicates a two-component structure that is consistent with our results from Voigt-profile fitting. Integration of the corrected apparent column density indicates a total column density of $\log N(\text{Si II}) = 13.96 \pm 0.02$, which is in good agreement with our Voigt-profile line-fitting values of $14.00(-0.07, +0.12)$.

absorber, some self-shielding could occur and affect the ionization of the gas, but this can also be explored with CLOUDY. Our modeling goal is to test whether we can explain all of the measured column densities, treating each component individually but assuming that each component has the same overall metallicity and the same relative abundances. We model the absorber as a plane-parallel, constant density slab photoionized by an external radiation field. Many galaxies are found within projected distances of a few hundred kiloparsecs of the sightline (see §2), so we assume that the ionizing flux field impinging on the absorber is dominated by flux emerging from these galaxies. We approximate the flux field with that of the midplane Milky Way radiation field modeled by Fox et al. (2005).³ In photoionization models, the degree of gas ionization depends on the ionization parameter U (\equiv ionizing photon density/particle number density), and the overall abundances depend on the assumed metallicity and relative abundance patterns (e.g., N/Si); we initially adopted solar relative abundances, but as we discuss below, we find

³ We also examined models in which the gas is ionized by the UV background from QSOs (Haardt & Madau 1996, 2012). The result is that our primary findings (regarding the abundances of N, Mg, and Si) did not change significantly; these various radiation fields have similar shapes near the ionization energies of the relevant nitrogen, magnesium, and silicon ions, so the models are insensitive to assumptions about the source of the ionizing UV flux.

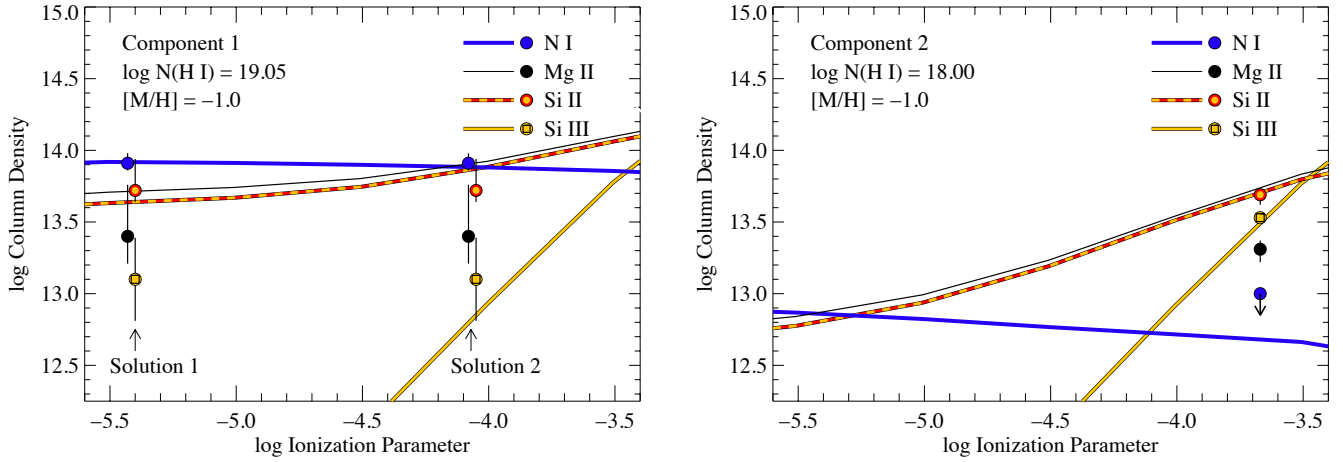


Figure 8. Photoionization models fitted to the measured column densities in component 1 (left panel) and component 2 (right panel) of the sub-DLA in the spectrum of PG 1543+489. For the models shown in this figure, we assume that the relative abundances are the same as those observed in the photosphere of the Sun (from [Asplund et al. 2009](#)) and there is no depletion of N, Mg, or Si by dust. The column densities predicted by the CLOUDY models are shown as a function of the ionization parameter. Model column densities are shown with smooth curves, and the observed column densities (from Table 2) are indicated with discrete symbols. For the stronger and more neutral component 1, we discuss multiple ways that the observed column densities could be interpreted in the context of this model; the two options that we discuss are labeled as “Solution 1” and “Solution 2” in the left panel.

that some departures from solar relative abundances are required. To fit the observed column densities, we vary the model $N(\text{H I})$, ionization parameter, and the overall metallicity in each component until the model column densities agree with the observed values within their 1σ uncertainties. We model each of the absorber components separately to allow for differing physical conditions, but we require the total H I column density, summed over both components, to equal the observed value, and we require that both components have the same metallicity since they are close in velocity and likely arise in regions that are close in space.

We initially attempted to fit the observed column densities with an overall metal abundance $[\text{M}/\text{H}]$ equal to the $[\text{N}/\text{H}]$ abundance reported above and with the relative gas-phase abundances of N, Mg, and Si fixed to the solar relative abundances. Figure 8 shows the outcome of this photoionization modeling for component 1 (left panel) and component 2 (right panel). As expected, the model N I column density changes only slightly as U increases; as long as the N I absorption arises in the inner region where the gas is mostly neutral, ionization corrections will be small for N I. On the other hand, $N(\text{Si III})$ increases dramatically with U as the surface of the gas slab becomes more and more ionized. We see that $N(\text{Si II})/N(\text{N I})$ also has an appreciable dependence on the ionization parameter; as U increases, more and more of the Si II absorption originates in the ionized gas on the slab surface where all of the nitrogen is in the N II stage (or higher).

For Si II and Si III, we see from Figure 8 that the photoionization models offer a variety of solutions. We first consider the models for component 1. At low U values such as the model with $\log U = -5.4$ labeled as “Solution 1” in Figure 8, ionization corrections are negligible, so, as we expect, the

model shows $N(\text{Si II})/N(\text{N I}) \approx (\text{Si}/\text{N})_{\odot}$. However, at $U = -5.4$, we would not expect to detect any Si III absorption. Thus, if the Si II and N I absorption only occurs in the neutral region such as at this Solution 1, then the Si III can only be understood by invoking some separate, more highly ionized Si III phase that has a low-enough $N(\text{H I})$ so that it does not appreciably affect the damping wings of the Ly α profile. The Si III phase also must be sufficiently ionized so that it contributes little to the Si II column but is not so ionized that it leads to detectable C IV lines (see below). Although this is physically plausible, it requires some fine tuning. Moreover, we also see that a higher ionization parameter such as “Solution 2” ($\log U \approx -4.1$) would produce enough Si III, so a simpler model of a gas slab with an ionized surface more fully agrees with the observed data. In this simpler model, $\log U$ cannot exceed ≈ -3.8 or the model will produce too much Si II and Si III.

The absence of N I in component 2 suggests that this component is more highly ionized or has a significantly lower $N(\text{H I})$ than component 1 (or both), and this is supported by the photoionization modeling presented in the right panel of Figure 8: we see that the silicon ion column densities and the absence of N I in component 2 can be easily satisfied with a photoionization model that has the same gas metallicity as component 1 but a significantly higher ionization parameter ($\log U \approx -3.7$). We note that a lower resolution spectrum of PG1543+489 obtained by [Borthakur et al. \(2013\)](#) shows no evidence of C IV in this absorption system. This is consistent with our photoionization models, which predict that $\log N(\text{C IV}) \ll 12$ even at the highest values of U shown in Figure 8. The absence of C IV also suggests that the absorber does not harbor substantial amounts of $\approx 10^5$ K plasma, but a higher resolution spectrum is required to place stringent lim-

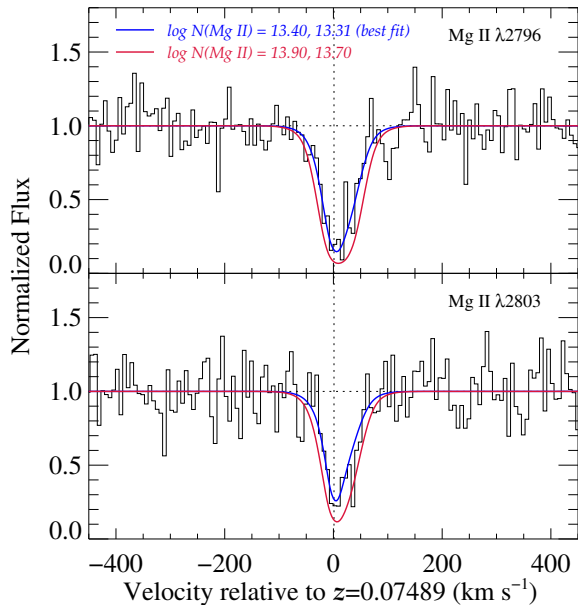


Figure 9. Voigt profiles for a two-component model of Mg II. The blue line shows the best-fit profile using the column densities and Doppler parameters listed in Table 2, and is the same as that drawn in Figure 6; the red line shows the profile assuming $\log N(\text{Mg II}) = 13.90$ and 13.70 , the approximate values required to better match $N(\text{Mg II})$ to the CLOUDY models in Figure 8. The latter model clearly produces stronger absorption than is observed.

its on C IV. A *Far Ultraviolet Spectroscopic Explorer* spectrum of PG1543+489 does not show significant absorption from O VI at the absorber redshift, but the data are noisy.

However, our best measurements of the observed Mg II column densities (black circles in Figure 8) are not well fitted in this model. In component 1, $N(\text{Mg II})$ has a large uncertainty because this component is deep and slightly saturated, and we see that the model is marginally consistent with the measured Mg II column within our estimated uncertainties if we choose Solution 1. However, this solution does not explain the observed Si III. If we choose Solution 2 instead, then the model Mg II column is considerably higher (by ≈ 0.5 dex) than the observed column. Moreover, in component 2 an even more severe discrepancy between the model and observed $N(\text{Mg II})$ is found at all values of U .

A possible explanation for the lower than expected Mg II column density might simply be that our profile fitting of the lines (§3) underestimates the true value of $N(\text{Mg II})$. To demonstrate that this is not likely to be the case, we show in Figure 9 profiles (in red) with values of $N(\text{Mg II})$ set to better match the CLOUDY solutions shown in Figure 8, $\log N(\text{Mg II}) = 13.90$ and 13.70 . The figure shows that the increased column density produces theoretical line profiles that no longer fit the data. Of course, the profiles are constructed assuming the same b and v values listed in Table 2. As a test, we refit all of the detected metal lines listed in Table 2, allowing b , v and N to vary, except that the values of $N(\text{Mg II})$ were

fixed to the higher values. The values of b , v , and N changed very little as a result, since the model is strongly constrained by the (higher signal-to-noise ratio) N I and Si II lines. We conclude that the value of $N(\text{Mg II})$ in Table 2 is robust and does not match the predicted CLOUDY models in Figure 8.

Compared to CLOUDY models, it appears that our data indicate that magnesium is underabundant (compared to solar) in this sub-DLA. At first glance, one might argue that this could be explained with some amount of depletion of magnesium and silicon by dust, with the Mg preferentially more depleted than the Si. Indeed, the Milky Way ISM dust depletion patterns reported by *Savage & Sembach (1996, their Figure 6)* generally show Mg to be ≈ 0.3 dex more depleted than Si, which is about the right amount to explain the Mg discrepancy in Figure 8. However, to overcome the debilitating saturation of the Mg II $\lambda\lambda 2796.35, 2803.53$ doublet that occurs in the Milky Way ISM, *Savage & Sembach (1996)* relied on the much weaker Mg II $\lambda\lambda 1239.93, 1240.40$ lines.⁴ After the *Savage & Sembach (1996)* depletion patterns were published, *Fitzpatrick (1997)*, *Theodosiou & Federman (1999)*, and *Sofia et al. (2000)* presented compelling observational and theoretical evidence that the Mg II $\lambda\lambda 1239.93, 1240.40$ oscillator strengths should be lowered by a factor of 2. This adjustment erases the preferential depletion of Mg in the *Savage & Sembach (1996)* patterns, i.e., after this adjustment, the dust depletion of Mg and Si is expected to be almost identical (see also *Jenkins 2009*). This appears to be true for dust in the Small Magellanic Cloud (SMC) as well, although the number of magnesium measurements along SMC sightlines is small (*Jenkins & Wallerstein 2017*).

We note that we have not used the original Ca II measurements in the PG 1543+489 sub-DLA (from *Bowen et al. 1991*) because those measurements have insufficient spectral resolution to distinguish the two components, but we note that the lower limit on $N(\text{Ca II})$ reported by *Bowen et al.* is easily consistent with the Ca II column densities expected in these photoionization models. In addition, our STIS observations cover the S II 1250 and 1253 Å lines, and since sulfur is an α -element, these lines potentially provide an important measure of the abundance. Unfortunately, the upper limit for $N(\text{S II})$ (Table 2) is too insensitive to provide a useful constraint.

5. SUMMARY AND DISCUSSION

As discussed in §1, we reobserved the PG 1543+489 sub-DLA to seek insight into its unusual characteristics (e.g., detection of Ca II at a relatively large impact parameter in the CGM), but our new data have raised new questions. In this section, we first briefly discuss some ideas about the nature of the absorber, and then provide some remarks about how these ideas could be tested with future observations. Before interpreting the data and discussing the nature of this absorption

⁴ The Mg II $\lambda\lambda 1239.93, 1240.40$ doublet is much too weak to be detected in the sub-DLA of PG 1543+489.

system, we summarize that it has the following characteristics:

1. The absorber is located in a galaxy group, with five known galaxies within a projected distance of 160 kpc and 21 galaxies within a radius of 10 Mpc and ± 500 km s⁻¹. The closest galaxy is a luminous, edge-on spiral galaxy (G1) at $\rho = 66$ kpc, and moreover, the QSO sightline is close to the major axis of G1. A second luminous spiral galaxy (G2) is found at $\rho = 119$ kpc. G1 and G2 are the brightest spirals in the group, and they, and the sub-DLA, are all offset to lower velocities than the bulk of the galaxies in the group. Hence, these objects may be moving into the group for the first time. Although we do find some “fuzz” near the QSO that could, in principle, be related to the absorption system, the redshift information (based on the detection of four emission lines in Q1543–K1) indicates that this fuzz is related to the QSO host.
2. A comparison of the velocity of the absorption system to the rotation curve of the nearby galaxy G1 indicates that the absorber could arise in a large gas disk that corotates with the stellar disk of that galaxy. The absorber velocity is lower than an extension of the flat part of the galaxy’s rotation curve, but that could be due to a Keplerian decrease in the rotation velocity at larger radii. Alternatively, this could indicate that the gas is in a rotating gas disk but also has an inflow component. Several other studies have reported similar evidence that galaxies have large rotating gas disks with declining rotation velocities at larger distances (Steidel et al. 2002; Ellison et al. 2003; Bowen et al. 2016; Ho et al. 2017).
3. We detect N I, Mg II, Si II, and Si III absorption along with a sub-damped H I Ly α absorption line, and we fitted two-component Voigt profiles to the metal-line data. The N I and H I indicate an overall metallicity of $[N/H] = -1.0 \pm 0.1$, or $\simeq 0.1 Z_{\odot}$. Photoionization models can explain the observed Si II and Si III in both components with the same metallicity, but the Mg II indicates that magnesium in the absorber is underabundant compared to the model expectations.

If we accept the photoionization modeling results for silicon and nitrogen at face value, then this sub-damped absorber presents some puzzling characteristics. The sub-DLA nitrogen abundance is almost an order of magnitude lower than the metallicity determined from the H II region emission lines observed in G1. This is not unprecedented, however: using COS observations of the QSO PG 1630+377, Ribaud et al. (2011) have reported a similar CGM absorber with a metallicity that is a factor of ≈ 30 lower than the metallicity of its closest galactic companion at $\rho = 37$ kpc. Ribaud et al. (2011) suggested that this metallicity discrepancy could indicate that the low-metallicity absorber is an example of the long-sought “cold-accretion” mode (Kereš et al. 2005)

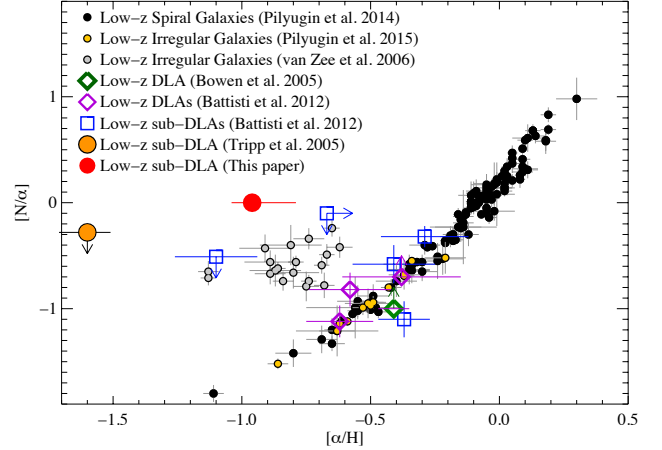


Figure 10. Comparison of the unusual abundance pattern in the PG 1543+489 sub-DLA (filled red circle) to abundance measurements in galaxies from van Zee & Haynes (2006), Pilyugin et al. (2014), and Pilyugin et al. (2015) and to abundance measurements in comparably low-redshift sub-DLAs and DLAs from Battisti et al. (2012), Bowen et al. (2005), and Tripp et al. (2005). The relative abundance of nitrogen compared to an α -group element is plotted vs. the overall α -group abundance. Given its low $[\alpha/H]$ value, it is somewhat surprising to find that the $[N/\alpha]$ is approximately solar.

of galaxy gas acquisition. It is interesting that the sub-DLA shows kinematical signatures of cold accretion, according to some theoretical works on how cold accretion would occur (Stewart et al. 2011, 2013). Indeed, a gradient of only -0.014 dex kpc⁻¹ is needed to match the galaxy’s metallicity to that of the DLA, if indeed the disk could be thought of as extending out to 66 kpc. This is well within the range of metallicity gradients for galaxy disks at all redshifts (e.g. Carton et al. 2018, and references therein).

Thus, the large discrepancy between the metallicities of the sub-DLA absorber and galaxy G1 are not necessarily problematic. The puzzling part is the apparent consistency of the $[N/\alpha]$ relative abundance⁵ with the solar value given the low overall level of metal enrichment of the absorber. To show why this is unusual, in Figure 10 we compare the PG 1543+489 sub-DLA abundance (large red circle) to abundances in low-redshift galaxies and other low- z DLAs and sub-DLAs (see the legend in the upper-left corner). As we can see from this figure, unlike the PG 1543+489 sub-DLA, most low- z galaxies and DLA/sub-DLA absorption systems have moderately to significantly subsolar $[N/\alpha]$ relative abundances when the overall metallicity is $\approx 0.1 Z_{\odot}$.

One hypothesis that could explain this unusual abundance pattern is that we have found an example of the “gas recycling” predicted by some theoretical studies of the baryon cycle (e.g., Ford et al. 2013). In this scenario, the gas could have

⁵ In this discussion, we are using silicon as a representative broader group of “ α ” elements. Silicon is often used in the literature as a typical α element.

been originally ejected from its galaxy of origin (perhaps G1) with a much higher overall metallicity, which would also explain the high $[N/\alpha]$ relative abundance. If that ejected gas subsequently mixed with rather metal-poor/pristine material in the CGM or the intragroup medium, the mixing might mainly add hydrogen to the absorber, which could reduce the overall metallicity without changing the $[N/\alpha]$ abundance by much. Given the observed kinematical correspondence of the absorber with the nearby galaxy, in this scenario the recycled gas would have now settled into the gas disk and will eventually feed into the stellar region of G1.

This hypothesis does not offer an easy explanation of the apparent underabundance of Mg compared to Si, however. Magnesium and silicon are both considered to be α -group elements, and in stellar populations, these elements become overabundant compared to iron as the metallicity decreases (e.g., McWilliam 1997), which is a result of the different nucleosynthetic origins of Mg and Si compared to Fe. The magnitude of the overabundance of Mg and Si is not always the same in low-metallicity gas, but unfortunately, the stellar abundance patterns of these two elements go in the wrong direction to explain the PG 1543+489 sub-DLA abundances: in low-metallicity objects, Mg is sometimes observed to be more abundant than Si (McWilliam 1997; Prochaska et al. 2000). It is possible that the underabundance of Mg is due to preferential depletion of Mg by dust, but in the most recent studies, Mg and Si are found to be depleted by dust in very similar amounts (e.g., Jenkins 2009); there is no strong evidence that Mg is preferentially depleted (compared to Si) in other contexts.

An explanation for the origin of the gas (albeit one that does not remedy the discrepant Mg/Si ratio) is that the sightline intercepts debris that arises from interactions between galaxies in the group, particularly between G1 and G2, which are of similar mass and could, at least in principle, constitute part of a major interaction. If the gas is dominated by material from a galaxy other than G1, it could have properties that differ from what we found from the emission lines associated with G1, as described in §2.2.1. Moreover, this gas could contain dust, which would be responsible for lowering the gas-phase abundance of Si but not N. If Si were depleted by -0.3 dex, our observation would be consistent with a true (total) value $[\alpha/H] = -0.7$, instead of -1.0 , and $[N/\alpha] = -0.3$. This condition would still be consistent with our ionization modeling discussed in §4 and would create an outcome in Figure 10 near the locus of points belonging to the results of van Zee & Haynes (2006) for low- z irregular galaxies. Going further, a depletion of Si equal to -0.65 dex would create the illusion that $[Si/H]$ (and hence $[\alpha/H]$) equals -1.0 , while in reality the value is -0.35 . Under this circumstance, $[N/\alpha] = -0.65$, and this possibility would be consistent with a point on the sequence of outcomes for low- z spiral and irregular galaxies determined by Pilyugin et al. (2014, 2015). Both choices would be consistent with our secure determination that $[N/H] = -1.0$.

One of the most detailed high $N(\text{H I})$ maps of a nearby interacting galaxy group comes from 21 cm observations

of the M81 triplet (Yun et al. 1994; de Blok et al. 2018), which offers a possible comparison with the group toward PG 1543+489. These data show how interacting galaxies can distribute high $N(\text{H I})$ gas over many tens of kiloparsecs on the sky, akin to the distances between the sightline toward PG 1543+489 and G1, G2, and G86. Absorption from an interacting group might be expected to be complex, spanning several hundred km s^{-1} , from clouds in different regions of the debris, as observed toward the line of sight of SN 1993J, which arose in M81 (de Boer et al. 1993; Bowen et al. 1994). We see no evidence for complex absorption toward PG 1543+489, but the environment intercepted by the sightline to SN 1993J was very different from that toward PG 1543+489, passing through the ISM and CGM of a spiral arm of M81 itself. In addition, the kinematics of any absorbing gas from tidal debris will depend on the orientation of the interaction on the plane of the sky, which is unknown for the galaxies toward PG 1543+489. Instead, our simple absorption-line component structure better matches the $5 - 10 \text{ km s}^{-1}$ dispersion of the 21 cm emission seen in the outer regions of M81, away from the centers of the galaxies (see, e.g. Figure 5 of de Blok et al. 2018). Similarly, the velocity of the absorption toward PG 1543+489 is $\sim -50 \text{ km s}^{-1}$ from the systemic velocity of G1 (Figure 3), which is consistent with that of 21 cm emission velocities toward various regions of the M81 triplet.

The existing data provide no definitive answer as to whether tidal debris is the origin of the absorption toward PG1543+489. The biggest problem with the hypothesis is the discrepancy of nearly 1 dex between the absorption-line abundance and the metallicity of the ISM gas in G1 derived from its emission lines (§2). To first order, we would expect gas ripped from G1 as a result of an interaction to have a similar abundance to that which we measure in its disk. This discrepancy alone is not inconsistent with assigning interactions with G1 as the primary origin of the absorption. For example, the metallicities of any gas that might contribute to the absorption from G2 and G86 are unknown, and although galaxies within a group might be expected to share star formation histories, data are required to measure whether their disks and/or CGM have different metallicities. Mixing of gas between two (or more) group galaxies with different metallicities, and with the IGM in which the group resides, could result in the deprecation of gas abundances in the outer regions of tidal debris complexes. Unfortunately, modeling whether such mixing could account for the lower abundances (or for the discrepant Mg/Si ratio discussed above) is beyond the scope of this paper.

Future observations of well-detected (but not saturated) O I lines would establish the overall α -element metallicity and remove the ambiguity caused by possible depletions by dust. If the oxygen abundance is higher and therefore $[N/\alpha]$ is subsolar, that would change our interpretation of the abundance patterns. Likewise, observations of species that tend to be more severely depleted by dust (e.g., iron or nickel) would be highly beneficial for sorting out whether the abundance patterns are due to dust depletion or to the nucleosynthetic

origin and chemical evolution of the gas. Better constraints on more highly ionized species would provide valuable constraints on whether confusion from ionization effects in a multiphase entity are an important factor. Also, the QSO is bright enough for the optical lines of Ca II and Na I to be recorded at echelle-like resolutions from the ground, which would better constrain the multicomponent model. Higher spatial resolution images of the galaxies might provide evidence for galaxy interactions through the detections of disturbed galaxy morphologies and/or tidal tails (and allow a more detailed study of the fuzz around the QSO, which we have associated with its host).

We appreciate helpful discussions with Celine Peroux and the use of custom-built 3D visualization software written by Bettie Stobie. B. L. F. acknowledges partial funding as an Invited Professor at the Université de Paris-Sud, Institute d'Astrophysique Spatial d'Orsay in 2016. B. L. F. is grateful also for partial funding at the Institute for Advanced Study in Princeton, and for hospitality at Princeton University in summer 2015. Support was provided for D. V. B. through grant GO-08625.01 from the Space Telescope Science Institute (STScI), which is operated by the Association of Universities for Research in Astronomy, Inc., under NASA contract NAS5-26555.

REFERENCES

- Aoki, W., Honda, S., Beers, T. C., Kajino, T., Ando, H., Norris, J. E., Ryan, S. G., Izumiura, H., Sadakane, K., & Takada-Hidai, M. 2005, *ApJ*, 632, 611
- Asplund, M., Grevesse, N., Sauval, A. J., & Scott, P. 2009, *ARA&A*, 47, 481
- Battisti, A. J., Meiring, J. D., Tripp, T. M., Prochaska, J. X., Werk, J. K., Jenkins, E. B., Lehner, N., Tumlinson, J., & Thom, C. 2012, *ApJ*, 744, 93
- Bell, E. F., McIntosh, D. H., Katz, N., & Weinberg, M. D. 2003, *ApJS*, 149, 289
- Bielby, R., Crighton, N. H. M., Fumagalli, M., Morris, S. L., Stott, J. P., Tejos, N., & Cantalupo, S. 2017, *MNRAS*, 468, 1373
- Birnboim, Y., & Dekel, A. 2003, *MNRAS*, 345, 349
- Borthakur, S., Heckman, T., Strickland, D., Wild, V., & Schiminovich, D. 2013, *ApJ*, 768, 18
- Borthakur, S., Heckman, T., Tumlinson, J., Bordoloi, R., Thom, C., Catinella, B., Schiminovich, D., Davé, R., Kauffmann, G., Moran, S. M., & Saintonge, A. 2015, *ApJ*, 813, 46
- Borthakur, S., Momjian, E., Heckman, T. M., Catinella, B., Vogt, F. P. A., & Tumlinson, J. 2018, arXiv: 1812.01632
- Borthakur, S., Momjian, E., Heckman, T. M., York, D. G., Bowen, D. V., Yun, M. S., & Tripp, T. M. 2014, *ApJ*, 795, 98
- Borthakur, S., Tripp, T. M., Yun, M. S., Bowen, D. V., Meiring, J. D., York, D. G., & Momjian, E. 2011, *ApJ*, 727, 52
- Bouché, N., Murphy, M. T., Kacprzak, G. G., Péroux, C., Contini, T., Martin, C. L., & Dessauges-Zavadsky, M. 2013, *Science*, 341, 50
- Bowen, D. V., Blades, J. C., & Pettini, M. 1995, *ApJ*, 448, 634
- Bowen, D. V., Chelouche, D., Jenkins, E. B., Tripp, T. M., Pettini, M., York, D. G., & Frye, B. L. 2016, *ApJ*, 826, 50
- Bowen, D. V., Jenkins, E. B., Pettini, M., & Tripp, T. M. 2005, *ApJ*, 635, 880
- Bowen, D. V., Jenkins, E. B., Tripp, T. M., Sembach, K. R., Savage, B. D., Moos, H. W., Oegerle, W. R., Friedman, S. D., Gry, C., Kruk, J. W., Murphy, E., Sankrit, R., Shull, J. M., Sonneborn, G., & York, D. G. 2008, *ApJS*, 176, 59
- Bowen, D. V., Pettini, M., Penston, M. V., & Blades, C. 1991, *MNRAS*, 249, 145
- Bowen, D. V., Roth, K. C., Blades, J. C., & Meyer, D. M. 1994, *ApJL*, 420, L71
- Bowen, D. V., Tripp, T. M., & Jenkins, E. B. 2001, *AJ*, 121, 1456
- Brandt, J. C., Heap, S. R., Beaver, E. A., Boggess, A., Carpenter, K. G., Ebbets, D. C., Hutchings, J. B., Jura, M., Leckrone, D. S., Linsky, J. L., Maran, S. P., Savage, B. D., Smith, A. M., Trafton, L. M., Walter, F. M., Weymann, R. J., Ake, T. B., Bruhweiler, F., Cardelli, J. A., Lindler, D. J., Malumuth, E., Randall, C. E., Robinson, R., Shore, S. N., & Wahlgren, G. 1994, *PASP*, 106, 890
- Burchett, J. N., Tripp, T. M., Bordoloi, R., Werk, J. K., Prochaska, J. X., Tumlinson, J., Willmer, C. N. A., O'Meara, J., & Katz, N. 2016, *ApJ*, 832, 124
- Burchett, J. N., Tripp, T. M., Wang, Q. D., Willmer, C. N. A., Bowen, D. V., & Jenkins, E. B. 2018, *MNRAS*, 475, 2067
- Butler, S. E., & Dalgarno, A. 1979, *ApJ*, 234, 765
- Carton, D., Brinchmann, J., Contini, T., Epinat, B., Finley, H., Richard, J., Patrício, V., Schaye, J., Nanayakkara, T., Weilbacher, P. M., & Wisotzki, L. 2018, *MNRAS*, 478, 4293
- Chengalur, J. N., Ghosh, T., Salter, C. J., Kanekar, N., Momjian, E., Keeney, B. A., & Stocke, J. T. 2015, *MNRAS*, 453, 3135
- Chisholm, J., Tremonti, C. A., Leitherer, C., Chen, Y., Wofford, A., & Lundgren, B. 2015, *ApJ*, 811, 149
- Davé, R., Oppenheimer, B. D., & Finlator, K. 2011, *MNRAS*, 415, 11
- de Blok, W. J. G., Walter, F., Ferguson, A. M. N., Bernard, E. J., van der Hulst, J. M., Neeleman, M., Leroy, A. K., Ott, J., Zschaechner, L. K., Zwaan, M. A., Yun, M. S., Langston, G., & Keating, K. M. 2018, *ApJ*, 865, 26
- de Boer, K. S., Pascual, P. R., Wamsteker, W., Sonneborn, G., Fransson, C., Bomans, D. J., & Kirshner, R. P. 1993, *A&A*, 280, L15
- Dekel, A., Birnboim, Y., Engel, G., Freundlich, J., Goerdt, T., Mumcuoglu, M., Neistein, E., Pichon, C., Teyssier, R., & Zinger, E. 2009, *Nature*, 457, 451

- Ellison, S. L., Mallén-Ornelas, G., & Sawicki, M. 2003, *ApJ*, 589, 709
- Ferland, G. J., Porter, R. L., van Hoof, P. A. M., Williams, R. J. R., Abel, N. P., Lykins, M. L., Shaw, G., Henney, W. J., & Stancil, P. C. 2013, *Rev. Mex. de Astron. y Astrofís.*, 49, 137
- Fitzpatrick, E. L. 1997, *ApJL*, 482, L199
- Ford, A. B., Oppenheimer, B. D., Davé, R., Katz, N., Kollmeier, J. A., & Weinberg, D. H. 2013, *MNRAS*, 432, 89
- Fox, A. J., Savage, B. D., & Wakker, B. P. 2005, *AJ*, 130, 2418
- Fumagalli, M., O’Meara, J. M., Prochaska, J. X., Rafelski, M., & Kanekar, N. 2015, *MNRAS*, 446, 3178
- Haardt, F., & Madau, P. 1996, *ApJ*, 461, 20
- . 2012, *ApJ*, 746, 125
- Ho, S. H., Martin, C. L., Kacprzak, G. G., & Churchill, C. W. 2017, *ApJ*, 835, 267
- Jenkins, E. B. 1996, *ApJ*, 471, 292
- . 2009, *ApJ*, 700, 1299
- Jenkins, E. B., & Wallerstein, G. 2017, *ApJ*, 838, 85
- Johnson, S. D., Chen, H.-W., Mulchaey, J. S., Tripp, T. M., Prochaska, J. X., & Werk, J. K. 2014, *MNRAS*, 438, 3039
- Kanekar, N., Neeleman, M., Prochaska, J. X., & Ghosh, T. 2018, *MNRAS*, 473, L54
- Kennicutt, R. C. 1998, *ARA&A*, 36, 189
- Kereš, D., Katz, N., Weinberg, D. H., & Davé, R. 2005, *MNRAS*, 363, 2
- Kewley, L. J., & Ellison, S. L. 2008, *ApJ*, 681, 1183
- Klitsch, A., Péroux, C., Zwaan, M. A., Smail, I., Oteo, I., Biggs, A. D., Popping, G., & Swinbank, A. M. 2018, *MNRAS*, 475, 492
- Kulkarni, V. P., Khare, P., Péroux, C., York, D. G., Lauroesch, J. T., & Meiring, J. D. 2007, *ApJ*, 661, 88
- López-Sánchez, Á. R., Dopita, M. A., Kewley, L. J., Zahid, H. J., Nicholls, D. C., & Scharwächter, J. 2012, *MNRAS*, 426, 2630
- López-Sanjuan, C., Díaz-García, L. A., Cenarro, A. J., Fernández-Soto, A., Viironen, K., Molino, A., Benítez, N., Cristóbal-Hornillos, D., Moles, M., Varela, J., Arnalte-Mur, P., Ascaso, B., Castander, F. J., Cerviño, M., González Delgado, R. M., Husillos, C., Márquez, I., Masegosa, J., Del Olmo, A., Pović, M., & Perea, J. 2018, *arXiv: 1805.03609*
- Maller, A. H., & Bullock, J. S. 2004, *MNRAS*, 355, 694
- Marino, R. A., Rosales-Ortega, F. F., Sánchez, S. F., Gil de Paz, A., Vílchez, J., Miralles-Caballero, D., Kehrig, C., Pérez-Montero, E., Stanishev, V., Iglesias-Páramo, J., Díaz, A. I., Castillo-Morales, A., Kennicutt, R., López-Sánchez, A. R., Galbany, L., García-Benito, R., Mast, D., Mendez-Abreu, J., Monreal-Ibero, A., Husemann, B., Walcher, C. J., García-Lorenzo, B., Masegosa, J., Del Olmo Orozco, A., Mourão, A. M., Ziegler, B., Mollá, M., Papaderos, P., Sánchez-Blázquez, P., González Delgado, R. M., Falcón-Barroso, J., Roth, M. M., van de Ven, G., & Califa Team. 2013, *A&A*, 559, A114
- McCourt, M., Sharma, P., Quataert, E., & Parrish, I. J. 2012, *MNRAS*, 419, 3319
- McWilliam, A. 1997, *ARA&A*, 35, 503
- Meiring, J. D., Lauroesch, J. T., Kulkarni, V. P., Péroux, C., Khare, P., & York, D. G. 2009, *MNRAS*, 397, 2037
- Monk, A. S., Penston, M. V., Pettini, M., & Blades, J. C. 1986, *MNRAS*, 222, 787
- Muzahid, S., Kacprzak, G. G., Churchill, C. W., Charlton, J. C., Nielsen, N. M., Mathes, N. L., & Trujillo-Gomez, S. 2015, *ApJ*, 811, 132
- Nestor, D. B., Pettini, M., Hewett, P. C., Rao, S., & Wild, V. 2008, *MNRAS*, 390, 1670
- Péroux, C., Dessauges-Zavadsky, M., D’Odorico, S., Kim, T.-S., & McMahon, R. G. 2003, *MNRAS*, 345, 480
- Péroux, C., Rahmani, H., Quiert, S., Pettini, M., Kulkarni, V., York, D. G., Straka, L., Husemann, B., & Milliard, B. 2017, *MNRAS*, 464, 2053
- Pettini, M., & Pagel, B. E. J. 2004, *MNRAS*, 348, L59
- Pettini, M., Zych, B. J., Steidel, C. C., & Chaffee, F. H. 2008, *MNRAS*, 385, 2011
- Pilyugin, L. S., Grebel, E. K., & Kniazev, A. Y. 2014, *AJ*, 147, 131
- Pilyugin, L. S., Grebel, E. K., & Zinchenko, I. A. 2015, *MNRAS*, 450, 3254
- Prochaska, J. X., Gawiser, E., Wolfe, A. M., Cooke, J., & Gelino, D. 2003, *ApJS*, 147, 227
- Prochaska, J. X., Naumov, S. O., Carney, B. W., McWilliam, A., & Wolfe, A. M. 2000, *AJ*, 120, 2513
- Rafelski, M., Wolfe, A. M., Prochaska, J. X., Neeleman, M., & Mendez, A. J. 2012, *ApJ*, 755, 89
- Rahmani, H., Péroux, C., Augustin, R., Husemann, B., Kacprzak, G. G., Kulkarni, V., Milliard, B., Møller, P., Pettini, M., Straka, L., Vernet, J., & York, D. G. 2018, *MNRAS*, 474, 254
- Ribaldo, J., Lehner, N., Howk, J. C., Werk, J. K., Tripp, T. M., Prochaska, J. X., Meiring, J. D., & Tumlinson, J. 2011, *ApJ*, 743, 207
- Rosenberg, J. L., Bowen, D. V., Tripp, T. M., & Brinks, E. 2006, *AJ*, 132, 478
- Rupke, D. S. N., & Veilleux, S. 2011, *ApJL*, 729, L27
- Savage, B. D., & Sembach, K. R. 1991, *ApJ*, 379, 245

- . 1996, *ARA&A*, 34, 279
- Schmidt, M., & Green, R. F. 1983, *ApJ*, 269, 352
- Sembach, K. R., & Savage, B. D. 1992, *ApJS*, 83, 147
- Sofia, U. J., Fabian, D., & Howk, J. C. 2000, *ApJ*, 531, 384
- Steidel, C. C., Kollmeier, J. A., Shapley, A. E., Churchill, C. W., Dickinson, M., & Pettini, M. 2002, *ApJ*, 570, 526
- Stewart, K. R., Brooks, A. M., Bullock, J. S., Maller, A. H., Diemand, J., Wadsley, J., & Moustakas, L. A. 2013, *ApJ*, 769, 74
- Stewart, K. R., Kaufmann, T., Bullock, J. S., Barton, E. J., Maller, A. H., Diemand, J., & Wadsley, J. 2011, *ApJ*, 738, 39
- Strauss, M. A., Weinberg, D. H., Lupton, R. H., Narayanan, V. K., Annis, J., Bernardi, M., Blanton, M., Burles, S., Connolly, A. J., Dalcanton, J., Doi, M., Eisenstein, D., Frieman, J. A., Fukugita, M., Gunn, J. E., Ivezić, Ž., Kent, S., Kim, R. S. J., Knapp, G. R., Kron, R. G., Munn, J. A., Newberg, H. J., Nichol, R. C., Okamura, S., Quinn, T. R., Richmond, M. W., Schlegel, D. J., Shimasaku, K., SubbaRao, M., Szalay, A. S., Vanden Berk, D., Vogeley, M. S., Yanny, B., Yasuda, N., York, D. G., & Zehavi, I. 2002, *AJ*, 124, 1810
- Strickland, D. K., Heckman, T. M., Colbert, E. J. M., Hoopes, C. G., & Weaver, K. A. 2004, *ApJS*, 151, 193
- Theodosiou, C. E., & Federman, S. R. 1999, *ApJ*, 527, 470
- Tripp, T. M., Jenkins, E. B., Bowen, D. V., Prochaska, J. X., Aracil, B., & Ganguly, R. 2005, *ApJ*, 619, 714
- Tripp, T. M., Meiring, J. D., Prochaska, J. X., Willmer, C. N. A., Howk, J. C., Werk, J. K., Jenkins, E. B., Bowen, D. V., Lehner, N., Sembach, K. R., Thom, C., & Tumlinson, J. 2011, *Science*, 334, 952
- van Dokkum, P. G. 2001, *PASP*, 113, 1420
- van Zee, L., & Haynes, M. P. 2006, *ApJ*, 636, 214
- Veilleux, S., Cecil, G., & Bland-Hawthorn, J. 2005, *ARA&A*, 43, 769
- Vila Costas, M. B., & Edmunds, M. G. 1993, *MNRAS*, 265, 199
- Voit, G. M., Meece, G., Li, Y., O’Shea, B. W., Bryan, G. L., & Donahue, M. 2017, *ApJ*, 845, 80
- Weiner, B. J., Coil, A. L., Prochaska, J. X., Newman, J. A., Cooper, M. C., Bundy, K., Conselice, C. J., Dutton, A. A., Faber, S. M., Koo, D. C., Lotz, J. M., Rieke, G. H., & Rubin, K. H. R. 2009, *ApJ*, 692, 187
- Wild, V., Hewett, P. C., & Pettini, M. 2007, *MNRAS*, 374, 292
- Wolfe, A. M., Gawiser, E., & Prochaska, J. X. 2005, *ARA&A*, 43, 861
- Woodgate, B. E., Kimble, R. A., Bowers, C. W., Kraemer, S., Kaiser, M. E., Danks, A. C., Grady, J. F., Loiacono, J. J., Brumfield, M., Feinberg, L., Gull, T. R., Heap, S. R., Maran, S. P., Lindler, D., Hood, D., Meyer, W., Vanhouten, C., Argabright, V., Franka, S., Bybee, R., Dorn, D., Bottema, M., Woodruff, R., Michika, D., Sullivan, J., Hetlinger, J., Ludtke, C., Stocker, R., Delamere, A., Rose, D., Becker, I., Garner, H., Timothy, J. G., Blouke, M., Joseph, C. L., Hartig, G., Green, R. F., Jenkins, E. B., Linsky, J. L., Hutchings, J. B., Moos, H. W., Boggess, A., Roesler, F., & Weistrop, D. 1998, *PASP*, 110, 1183
- Yun, M. S., Ho, P. T. P., & Lo, K. Y. 1994, *Nature*, 372, 530
- Zych, B. J., Murphy, M. T., Pettini, M., Hewett, P. C., Ryan-Weber, E. V., & Ellison, S. L. 2007, *MNRAS*, 379, 1409